nanomaterials

MDPI

Article

Facile Preparation of Three-Dimensional Cubic $MnSe_2$/CNTs and Their Application in Aqueous Copper Ion Batteries

Junjun Wang [1,2], Linlin Tai [3], Wei Zhou [2], Han Chen [2], Jingxiong Liu [1,*] and Shaohua Jiang [3,*]

[1] College of Liling Ceramic, Hunan University of Technology, Zhuzhou 412007, China
[2] Hunan Key Laboratory of Applied Environmental Photocatalysis, Changsha University, Changsha 410022, China; zhouwei_csu@163.com (W.Z.); 18900753550@163.com (H.C.)
[3] Jiangsu Co-Innovation Center of Efficient Processing and Utilization of Forest Resources, International Innovation Center for Forest Chemicals and Materials, College of Materials Science and Engineering, Nanjing Forestry University, Nanjing 210037, China
* Correspondence: liujingxiong@hut.edu.cn (J.L.); shaohua.jiang@njfu.edu.cn (S.J.)

Abstract: Transition metal sulfide compounds with high theoretical specific capacity and excellent electronic conductivity that can be used as cathode materials for secondary batteries attract great research interest in the field of electrochemical energy storage. Among these materials, $MnSe_2$ garners significant interest from researchers due to its unique three-dimensional cubic structure and inherent stability. However, according to the relevant literature, the performance and cycle life of $MnSe_2$ are not yet satisfactory. To address this issue, we synthesize $MnSe_2$/CNTs composites via a straightforward hydrothermal method. $MnSO_4 \cdot H_2O$, Se, and $N_2H_4 \cdot H_2O$ are used as reactants, and CNTs are incorporated during the stirring process. The experimental outcomes indicate that the fabricated electrode demonstrates an initial discharge specific capacity that reaches 621 mAh g^{-1} at a current density of 0.1 A g^{-1}. Moreover, it exhibits excellent rate capability, delivering a discharge specific capacity of 476 mAh g^{-1} at 10 A g^{-1}. The electrode is able to maintain a high discharge specific capacity of 545 mAh g^{-1} after cycling for 1000 times at a current density of 2 A g^{-1}. The exceptional electrochemical performance of the $MnSe_2$/CNTs composites can be ascribed to their three-dimensional cubic architecture and the 3D CNT network. This research aids in the progression of aqueous Cu-ion cathode materials with significant potential, offering a viable route for their advancement.

Keywords: aqueous battery; $MnSe_2$; carbon nanotubes; Cu-ion battery

Citation: Wang, J.; Tai, L.; Zhou, W.; Chen, H.; Liu, J.; Jiang, S. Facile Preparation of Three-Dimensional Cubic $MnSe_2$/CNTs and Their Application in Aqueous Copper Ion Batteries. *Nanomaterials* **2024**, *14*, 1621. https://doi.org/10.3390/nano14201621

Academic Editors: Christian Julien and Carlos Miguel Costa

Received: 17 September 2024
Revised: 5 October 2024
Accepted: 9 October 2024
Published: 10 October 2024

1. Introduction

Propelled by carbon-neutrality policies, the widespread adoption of renewable energy has become an inevitable direction for development. However, new energy sources, such as wind, solar, tidal, and geothermal energy, are limited by natural conditions such as climate, latitudinal location, topography, etc., and there is a serious imbalance between supply and demand in time and space. Therefore, the vigorous development of electrochemical energy storage systems is currently recognized as the most effective solution strategy, such as Zn-ion batteries [1], supercapacitor [2–4], Li-ion battery [5], ammonium-ion batteries [6–8], hybrid battery [9], microbial fuel cell [10], Li-S batteries [11], zinc-ion hybrid supercapacitors [12], and so on. Lithium-ion batteries are predominant across various types of energy storage technologies, particularly in applications involving new energy vehicles, electronic devices, and renewable energy storage systems. This dominance is attributed to their exceptional high energy density, robust power output capabilities, and well-established industrial production processes. These advantages have enabled lithium-ion batteries to exhibit significant competitiveness and reliability across a wide range of applications [13–15]. Despite the extensive application of lithium-ion batteries across various fields, their high costs and less-than-optimal safety performance have constrained the further development of this technology. In contrast, among the many battery technologies that have emerged in recent

years, aqueous ion batteries have rapidly gained research prominence and widespread attention. This is as a result of their cost-effectiveness, exceptional stability, superior safety features, and sustainability advantages [16,17]. Currently, a variety of metal ions, for example, Zn^{2+}, Na^{+}, K^{+}, Mg^{2+}, Cu^{2+}, and Al^{3+}, are being explored as charge carriers in conventional aqueous batteries [18,19]. Among these metals, copper (Cu) stands out due to its high reaction potential, impressive theoretical specific capacity (844 mA h/g and 7558 mA h/cm^3), and significant natural abundance [20,21].

Wu et al. [22] reported an innovative aqueous secondary battery utilizing Cu^{2+} as the charge carrier, demonstrating excellent redox activity for energy storage. Their findings revealed a sequential S-CuS-Cu_2S conversion mechanism in the sulfur electrode, facilitating a four-electron reaction process. The fabricated copper–sulfur cell exhibited a remarkable electrochemical performance, achieving a specific capacity of up to 3044 mAh g^{-1} at a current density of 100 mA g^{-1} and retaining 72% of its initial capacity after 1200 cycles at an elevated current density of 12.5 A g^{-1}. In addition, Zhang J. S. et al. [23] conducted a systematic investigation into the effects of anion exchange on the kinetic properties of $CuS_{1-x}Se_x$. By combining electrochemical analysis with structural and spectral studies, they highlighted that the anion exchange between S and Se in $CuS_{1-x}Se_x$ not only mitigated phase transitions but also enhanced electron and ion transport by reducing energy barriers. This improvement facilitated stable copper ion storage and significantly boosted electrochemical performance. Specifically, self-supported $CuS_{0.5}Se_{0.5}$ nanosheets delivered a specific capacity of up to 491 mAh g^{-1} and maintained 80% of their reversible capacity at a high current density of 20 A g^{-1}, outperforming CuS. Despite these advancements, the development of aqueous copper batteries remains in its early stages. Among these, the application of transition metal sulfide cathode materials in aqueous copper batteries is still in its initial stages of development. The key to their further development lies in the advancement of high-performance electrode materials and a deeper understanding of the mechanisms underlying copper ion energy storage.

In the contemporary research landscape, transition metal sulfide compounds have surfaced as potential options for energy storage applications because of their distinct chemical characteristics, including extensive redox chemistry, which enables a wide array of practical uses [24,25]. Among the various transition metal compounds, selenides and sulfides particularly excel due to their exceptional electrocatalytic activity, high electrical conductivity, and robust metal bonding characteristics [26,27]. Recently, extensive studies have been conducted on metal selenides and sulfides [28–35], demonstrating their substantial stability and performance in energy storage systems. Selenium (Se) exhibits lower ionization energy and better electrical conductivity compared to sulfur (S), making the substitution of Se for oxygen (O) atoms in manganese compounds a focal point for researchers [36]. Among these selenides, manganese diselenide distinguishes itself due to its low cost, low toxicity, and excellent catalytic properties. As a result, it is extensively used in electrode materials and oxygen reduction catalysts for lithium- and sodium-ion batteries. However, the application of manganese diselenide in aqueous copper-ion batteries remains unexplored. Therefore, the utilization of manganese diselenide as a cathode material for aqueous copper-ion batteries warrants investigation. Regrettably, manganese diselenide faces challenges such as sluggish kinetics and volume expansion [37]. To tackle these challenges, carbon-based materials, particularly one-dimensional carbon nanotubes (CNTs), are extensively utilized as conductive additives [38]. Owing to their distinctive cross-linking capabilities and disordered structural arrangement, carbon nanotubes enhance the mechanical stability of composite materials while simultaneously facilitating a broader distribution of active sites [39,40]. Consequently, incorporating carbon nanotubes into manganese-based compounds can greatly enhance the stability and electrical conductivity of these materials.

To improve the electrochemical performance of $MnSe_2$ cathode materials in aqueous copper ion batteries, we successfully synthesized $MnSe_2$/CNTs (MSCN) composites via a hydrothermal method. Se, $MnSO_4$, and CNTs served as the sources of selenium, manganese, and carbon, respectively. The CNTs were uniformly adhered to the surface of the

$MnSe_2$ cubes, effectively mitigating electrode volume expansion and improving copper ion conductivity. The MSCN composite shows an impressive starting discharge specific capacity of 621 mAh g^{-1} under a current density of 0.1 A g^{-1}. It also reveals a significant rate performance, sustaining a discharge specific capacity of 477 mAh g^{-1} when exposed to a current density of 10 A g^{-1}. Additionally, after 1000 cycles at a current density of 2 A g^{-1}, the composite maintains a high discharge specific capacity of 545 mAh g^{-1}. The MSCN cathode presents a promising avenue for rapid and durable copper ion storage.

2. Materials and Methods

2.1. Materials

Selenium powder (99.99%) and manganese sulfate monohydrate (99%) were sourced from Sinopharm Chemical Reagent Co. (Shanghai, China). Citric acid monohydrate (99.5%) and carbon nanotubes (≥95%) were acquired from Shanghai Aladdin Biochemical Technology Co. (Shanghai, China). Hydrazine hydrate (80%) was obtained from Hunan Huihong Reagent Co. Anhydrous ethanol was provided by Tianjin Fuyu Fine Chemical Industry (Tianjin, China), while acetylene black, polyvinylidene fluoride, and N-methyl pyrrolidone were procured from Advanced Technology Industry Corporation(Changsha, China). All solutions were prepared using distilled water as the solvent, and all raw materials employed were of analytical grade, used without further purification.

2.2. Synthesis of $MnSe_2$/CNTs Composites

Firstly, to synthesize the desired material, 0.338 g of manganese sulfate monohydrate, 0.3158 g of selenium powder, and 3 g of citric acid were dissolved in 44 mL of distilled water and stirred for 30 min. Following this, 16 mL of hydrazine hydrate were introduced to the mixture, followed by an additional hour of stirring to ensure thorough mixing. Concurrently, 50 mg of CNTs were introduced into the mixed solution and subjected to ultrasonication for 30 min, resulting in a homogeneous mixture. The solution was then placed into a 100 mL Teflon-lined autoclave and heated at 180 °C for a duration of 12 h. Once the autoclave had cooled to ambient temperature, the resulting black precipitate was collected and meticulously washed with distilled water and anhydrous ethanol. The cleaned precipitate was subsequently dried in a vacuum at 60 °C for 12 h. The final samples were labeled as MSCN. To facilitate comparison, the CNT quantity was varied to 20 mg and 80 mg, while keeping other conditions constant. These three samples were accordingly named MSCN-1, MSCN-2, and MSCN-3. In the absence of carbon nanotubes (CNTs), the synthesized sample consisted solely of $MnSe_2$.

2.3. Materials Characterizations

The composition and crystal structure of the synthesized samples were analyzed using X-ray diffraction (XRD) with a Rigaku ULTIMA IV X-ray powder diffractometer (Tokyo, Japan). The X-ray generator operated at 3 kW, with a Cu Kα radiation source (λ = 0.154056 nm). Continuous scanning was performed at a speed of 5°/min across a range from 10° to 90°.

The composition and chemical state of the synthesized samples were further examined by X-ray photoelectron spectroscopy (XPS), using a Thermo Fisher Scientific K-Alpha spectrometer (Waltham, MA, USA). The system employed an Al Kα source, with an excitation energy of 1486.8 eV, a test spot area adjustable between 50 and 400 μm (in 5 μm steps), a tube voltage of 15 kV, and a tube current of 10 mA. The data-acquisition step size was 0.05 eV, and the resulting spectra were analyzed using XPS PEAK 41 software. To investigate the morphology and microstructure of the samples and electrodes, scanning electron microscopy (SEM) and transmission electron microscopy (TEM) were utilized. SEM analysis was conducted using a Carl Zeiss Sigama 300 field emission SEM equipped with a backscattered electron probe (BSE) and an X-ray energy-dispersive spectrometer (EDS). TEM analysis was performed using a Tecnai G2 F20 field-emission high-resolution transmission electron microscope from FEI (Hillsboro, OR, USA).

2.4. Electrochemical Measurements

MSCN-1, MSCN-2, MSCN-3, and copper foil were utilized as working and counter electrodes, respectively. A cellulose membrane served as the separator, and the electrolyte was composed of 0.5 mol L^{-1} $CuSO_4$ solution. These components were assembled into a CR-2025 coin cell for subsequent electrochemical performance testing. The MSCN-x (x = 1, 2, 3), acetylene black, and polytetrafluoroethylene binder (PVDF) were homogeneously mixed in an 8:1:1 mass ratio, respectively. Subsequently, to facilitate the milling process, N-methyl pyrrolidone (NMP) was introduced as a solvent. Stainless steel was chosen as the current collector, upon which the aforementioned mixed slurry was uniformly applied. The coated substrate was then placed in a vacuum-drying oven, where it was maintained at 60 °C for a duration of 24 h to ensure thorough drying. Finally, the dried stainless-steel foil was punched into circular electrodes with a diameter of 12 mm, using a slicing machine, and the prepared electrodes and copper foil anodes were assembled into CR-2025 coin cells. Electrochemical tests, normalized to the mass of the active cathode material, were conducted using a CHI660E electrochemical workstation (Austin, TX, USA) and a Neware CT-4008T battery tester (Shenzhen, China).

3. Results and Discussion

A straightforward hydrothermal treatment approach was employed, utilizing a temperature of 180 °C for 12 h. In this process, $MnSO_4 \cdot H_2O$ and Se served as the sources of manganese and selenium, respectively, with the addition of carbon nanotubes during the stirring procedure. The uniform distribution of components in the solution facilitates the improved synthesis of $MnSe_2$/CNTs composites. The detailed synthesis procedure is depicted in Figure 1.

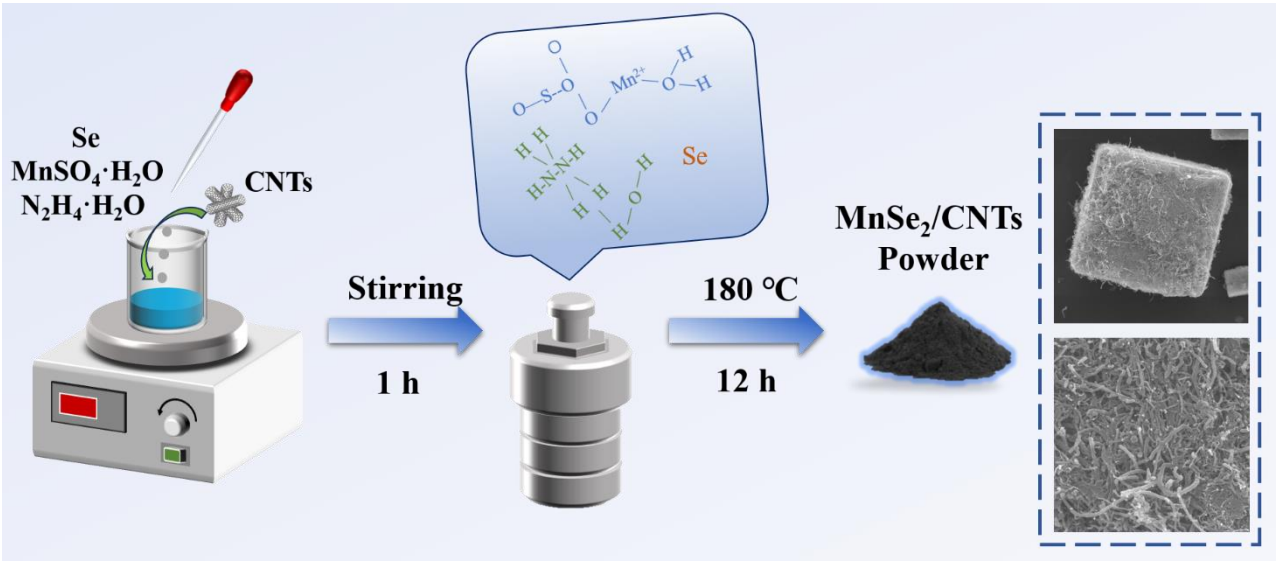

Figure 1. Diagrammatic representation of the fabrication process for MSCN-x (x = 1, 2, 3) composite structures.

The potential reactions occurring during the hydrothermal synthesis process are elucidated as follows:

$$MnSO_4 \cdot H_2O + 2N_2H_4 \cdot H_2O + 2Se \rightarrow MnSe_2 + (NH_4)_2SO_4 + 3H_2O + N_2\uparrow \quad (1)$$

In the hydrothermal reaction with Mn^{2+}, selenium powder was reduced by hydrazine hydrate, while citric acid primarily functioned to neutralize the excess alkaline hydrazine hydrate. MSCN-x (x = 1, 2, 3) was characterized and analyzed using X-ray diffraction (XRD) and X-ray photoelectron spectroscopy (XPS). As illustrated in Figure 2a, the X-ray

diffraction (XRD) patterns of the MSCN-x (x = 1, 2, 3) composite materials align precisely with the reference data (PDF#73-1525) [41]. The diffraction peaks observed at 24.27°, 27.78°, 31.14°, 34.19°, 39.69°, 42.21°, 46.92°, 49.14°, and 51.29° correspond to the (111), (200), (210), (211), (220), (221), (311), (222), and (023) crystallographic planes, respectively, indicating high crystallinity. The above analysis indicates that no significant impurity phases were detected, and the incorporation of carbon nanotubes did not interfere with the synthesis of $MnSe_2$. In addition to the crystalline surface corresponding to $MnSe_2$, a low-intensity amorphous bump around 24.5° is clearly observed, attributed to the (002) plane of amorphous carbon. No other noticeable impurity phases were detected in the pattern.

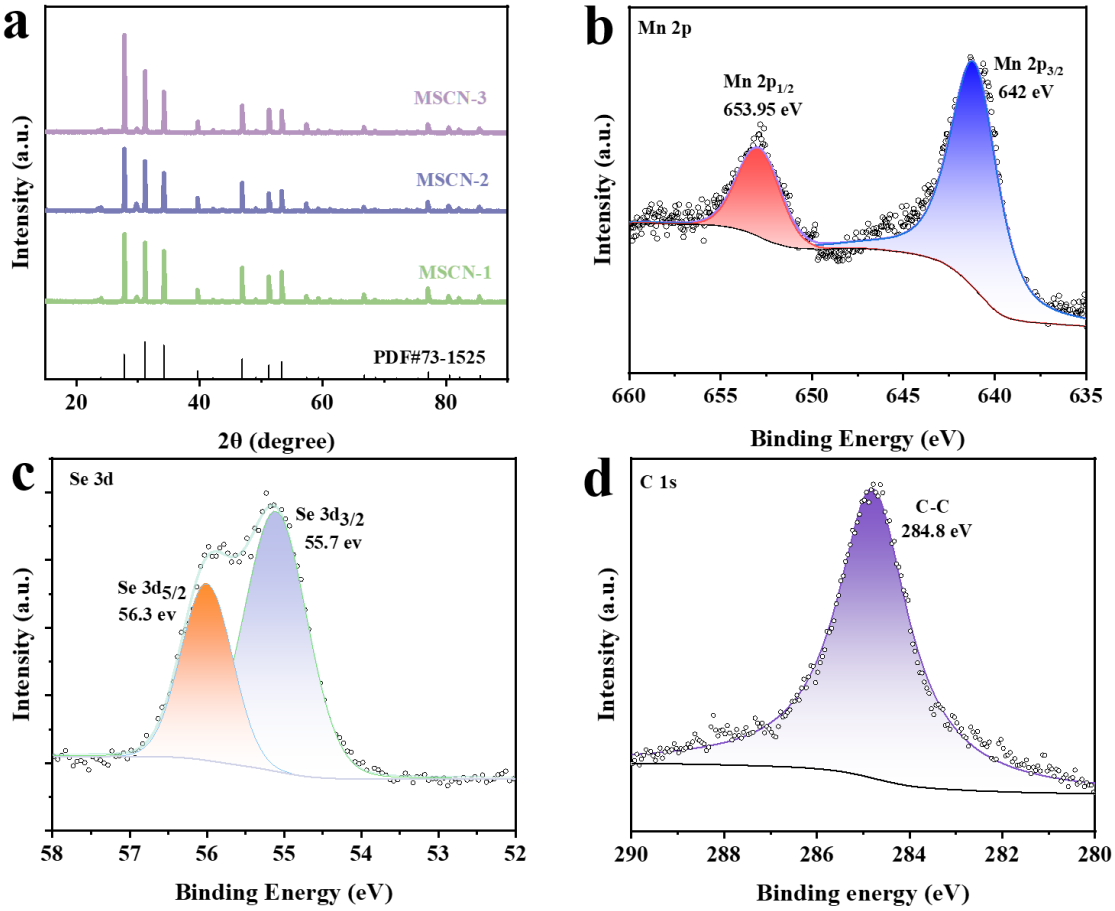

Figure 2. (**a**) XRD patterns of MSCN-1, MSCN-2, and MSCN-3. (**b**–**d**) High-resolution spectra of Mn 2p, Se 3d, and C 1s of the MSCN-2.

To gain a deeper understanding of the chemical-bonding states and elemental composition of the synthesized materials, the samples were analyzed by X-ray photoelectron spectroscopy (XPS), which is often used to measure the elemental composition, as well as the chemical and electronic state of the atoms of materials [42–45]. As shown in Figure 2b–d, the XPS results confirm the presence of Mn 2p and Se 3d elements, with carbon (C 1s) adsorbed on the surface. As depicted in Figure 2c, two prominent peaks were observed at 642 eV and 653.95 eV, corresponding to Mn $2p_{3/2}$ and Mn $2p_{1/2}$, respectively [46]. Figure 2d displays the Se elemental analysis, showing peaks at 55.7 eV (Se 3d5/2) and 56.3 eV (Se 3d3/2), which indicate a chemical bond between Mn and Se [47]. As presented in Figure 2d, the high-resolution C 1s spectrum detected at 284.8 eV signifies the presence of C-C bonds [48].

The morphology of MSCN-x (x = 1, 2, 3) was investigated with scanning electron microscopy (SEM), which is effective for investigating the surfaces of materials [49–51]. As illustrated in Figure 3a–f, the samples exhibit a distinctive micro-sized cubic morphology, with varying amounts of carbon nanotubes (CNTs) attached to their surfaces due to differ-

ences in CNT concentration. Figure 3c reveals that MSCN-3 exhibits agglomerated CNTs on its surface. In contrast, MSCN-1 displays a heterogeneous distribution with sparse CNTs, as illustrated in Figure 3a. Meanwhile, MSCN-2 demonstrates embedded homogeneous CNTs, as evidenced in Figure 3b. Upon closer examination, as illustrated in Figure 3f, significant CNT aggregation is evident in MSCN-3, which is likely contributing to the observed effects on electrochemical performance, as discussed in subsequent sections. In contrast, Figure 3d shows that the CNTs in MSCN-1 are not uniformly distributed on the cubes. Conversely, the surface of MSCN-2 in Figure 3e appears more homogeneous, with fewer CNTs aggregations, and this is a critical factor for its superior electrochemical performance. For a clearer and more intuitive comparison, Supplementary Figure S1 reveals that, without the addition of CNTs, the structure remains a clean cubic form. The inclusion of surface CNTs did not alter the intrinsic 3D $MnSe_2$ structure. The consistent homogeneity of CNTs in MSCN-2 is corroborated by multiple observations in these figures.

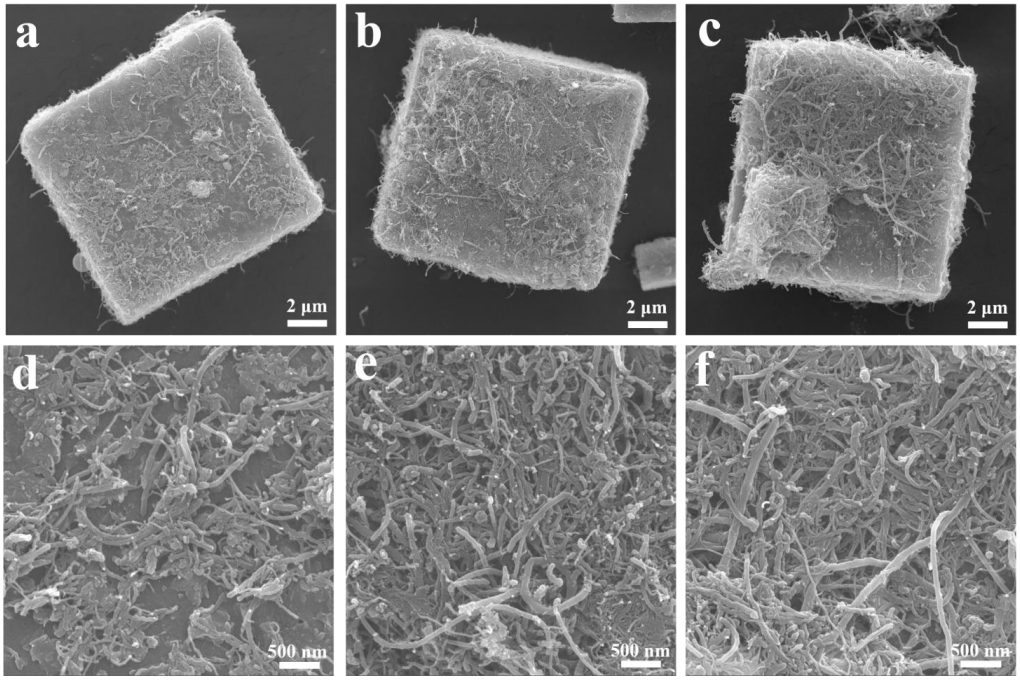

Figure 3. SEM images of (**a**,**d**) MSCN-1, (**b**,**e**) MSCN-2, and (**c**,**f**) MSCN-3.

These homogeneous CNTs provide more edges and faces, effectively increasing the overall surface area and thereby enhancing electrochemical performance. Transmission electron microscopy (TEM) analysis of MSCN-2, as depicted in Figure 4a–c, shows a distinct lattice spacing of 2.86 Å, which matches the (210) plane of $MnSe_2$, as confirmed by high-resolution TEM (Figure 4b). The patterns from selected-area electron diffraction (SAED) clearly show distinct diffraction rings, as depicted in Figure 4c, corresponding to the (221), (220), (211), and (210) planes of $MnSe_2$, respectively, which align perfectly with the XRD results, thus confirming the excellent crystallization of $MnSe_2$. Additionally, the elemental mapping of the MSCN-2 composites using energy-dispersive spectroscopy (EDS), as illustrated in Figure 4d, indicates a uniform distribution of Mn, Se, and C elements within MSCN-2. In addition, the energy-dispersive X-ray spectroscopy (EDS) image (Supplementary Figure S7) shows that the atomic ratio of Mn to Se is approximately 2:1, which is consistent with the results from elemental mapping. This homogeneous distribution significantly increases conductive pathways, mitigates volume expansion, facilitates electrolyte diffusion, and improves electron transfer, thereby enhancing the electrochemical storage capacity of the material.

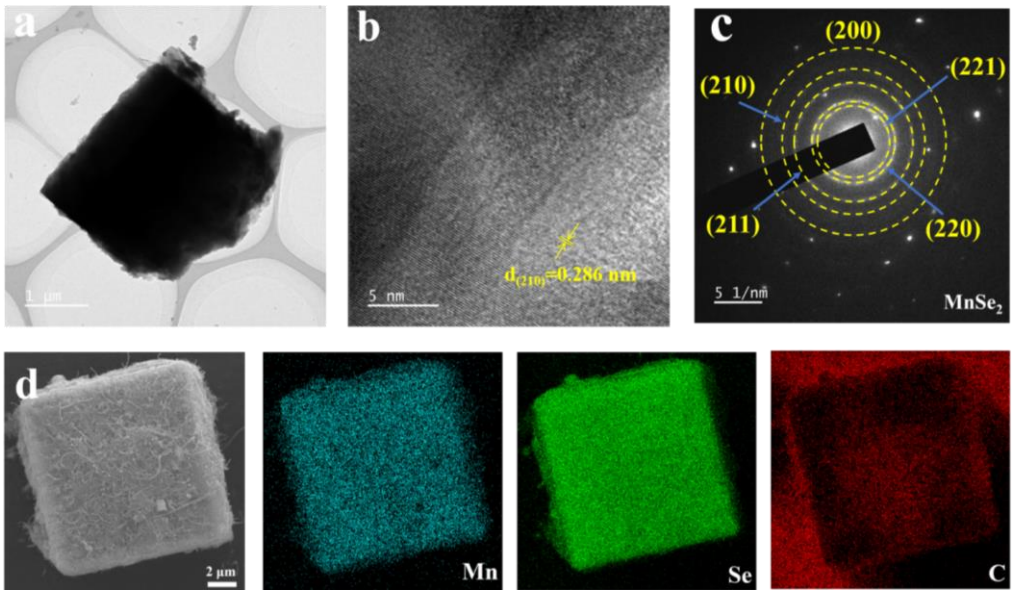

Figure 4. (**a**) HAADF-STEM images of the MSCN-2, (**b**) HR-TEM image, (**c**) SAED pattern, and (**d**) corresponding EDS elemental mapping of MSCN-2.

Cyclic voltammetry (CV) measurements of the MSCN-2 electrodes were conducted at a scan rate of 0.1 mV s^{-1}, as illustrated in Figure 5a. The cyclic voltammograms (CV) of the MSCN-1 (Supplementary Figure S2) and MSCN-3 (Supplementary Figure S3) electrodes exhibit similar characteristics to those observed in the MSCN-2 electrode. All CV curves displayed distinct oxidation–reduction peaks and exhibited similar profiles. Specifically, two pairs of pronounced anodic and cathodic peaks were observed near 0.14/0.25 V and 0.08/0.13 V, individually, which results from the reversible insertion and extraction of Cu^{2+} ions at the MSCN anode [52]. Moreover, the MSCN-2 electrode demonstrated higher peak currents at redox potentials compared to MSCN-1 and MSCN-3 electrodes, suggesting superior electrochemical activity, and such enhanced activity facilitates the kinetics of Cu^{2+} (de)insertion, thereby resulting in the highest specific capacity among the three electrodes. In Figure 5b, the initial charge and discharge profiles for MSCN-1, MSCN-2, and MSCN-3 at a current density of 0.1 A g^{-1} are depicted. A noticeable voltage plateau is evident in the 0~0.4 V range, which corresponds closely with the previously discussed CV results. Notably, the MSCN-2 electrode achieved an initial discharge specific capacity of 621 mAh g^{-1}, exceeding the specific capacities of MSCN-1 (612 mAh g^{-1}) and MSCN-3 (592 mAh g^{-1}). Figure S4 presents the charge/discharge curves of $MnSe_2$ for the initial three cycles at a current density of 0.1 A g^{-1}. The specific discharge capacities recorded were 585 mAh g^{-1} for the first cycle, 396 mAh g^{-1} for the second cycle, and 424 mAh g^{-1} for the third cycle. These values are lower than the specific discharge capacities of MSCN-1, MSCN-2, and MSCN-3. This evidence further underscores the significant role that CNT incorporation plays in enhancing the electrochemical performance of the material.

The rate performance of MSCN-1, MSCN-2, and MSCN-3 electrodes is depicted in Figure 5c. Among the three, the MSCN-2 electrode demonstrates a superior rate performance, maintaining an excellent discharge capacity across various current densities. The specific discharge capacities at current densities of 0.1, 0.5, 2, 5, 8, and 10 A g^{-1} were 622, 593, 570, 547, 517, and 476 mAh g^{-1}. While the multiplier performance of MSCN-1 and MSCN-3 was not satisfactory, the discharge specific capacity of MSCN-1 at the same multiplier current was 611, 559, 530, 491, 440, and 288 mAh g^{-1}, and that of MSCN-1 at the same multiplier current was 590, 549, 523, 481, 430, and 343 mAh g^{-1}. respectively. Notably, under elevated current densities (at 10 A g^{-1}), the discharge specific capacity of the MSCN-2 electrode significantly exceeded that of MSCN-1 (343 mAh g^{-1}) and MSCN-3 (286 mAh g^{-1}). Furthermore, upon reverting the current density back to 0.1 A g^{-1}, the

MSCN-2 electrode retained a discharge specific capacity of 615 mAh g^{-1}, while the discharge specific capacities of MSCN-1 and MSCN-3 under the same conditions were 571 and 559 mAh g^{-1}. These results demonstrate the excellent rate stability of the MSCN-2 electrode. Figure 5d illustrates the cycling performance of the MSCN-2 electrode when subjected to a current density of 2 A g^{-1}, showing reversible discharge specific capacities of 644, 608, 580, 569, and 544 mAh g^{-1} after 200, 400, 600, 800, and 1000 cycles, respectively. This indicates the excellent cycling stability of the MSCN-2 electrode. In comparison to the MSCN-1 and MSCN-3 electrodes, MSCN-2 exhibits superior long-term cycling performance when operated at a current density of 2 A g^{-1}, as illustrated in Figure 5e. Initially, the MSCN-x (x = 1, 2, 3) electrodes exhibit similar specific capacities, likely due to the gradual electrochemical activation process occurring within the MSCN electrodes [52]. Remarkably, following 200 cycles, the MSCN-2 electrode exhibits a substantially higher specific capacity compared to both MSCN-1 and MSCN-3. After 400 cycles, a sharp decline in specific capacity is observed for the MSCN-3 electrode. The post-cycled X-ray spectroscopy (EDS) image reveals a significant decrease in the elemental content of Mn and Se compared to pre-cycling levels, with Se and Mn percentages at 2.9% and 0.3%, respectively. This reduction may be the primary reason for the sudden decline in the capacity of the MSCN-3 electrode after 400 cycles. In contrast, the capacities of the MSCN-1 and MSCN-2 electrodes remain more stable. By the 1000th cycle, the specific capacity of the MSCN-3 electrode drops to 179 mAh g^{-1}, while the MSCN-1 and MSCN-2 electrodes retain specific capacities of 491 and 545 mAh g^{-1}, respectively. The moderate content of carbon nanotubes (CNTs) in the MSCN-2 electrode provides a distinct advantage, enabling it to achieve a high reversible specific capacity.

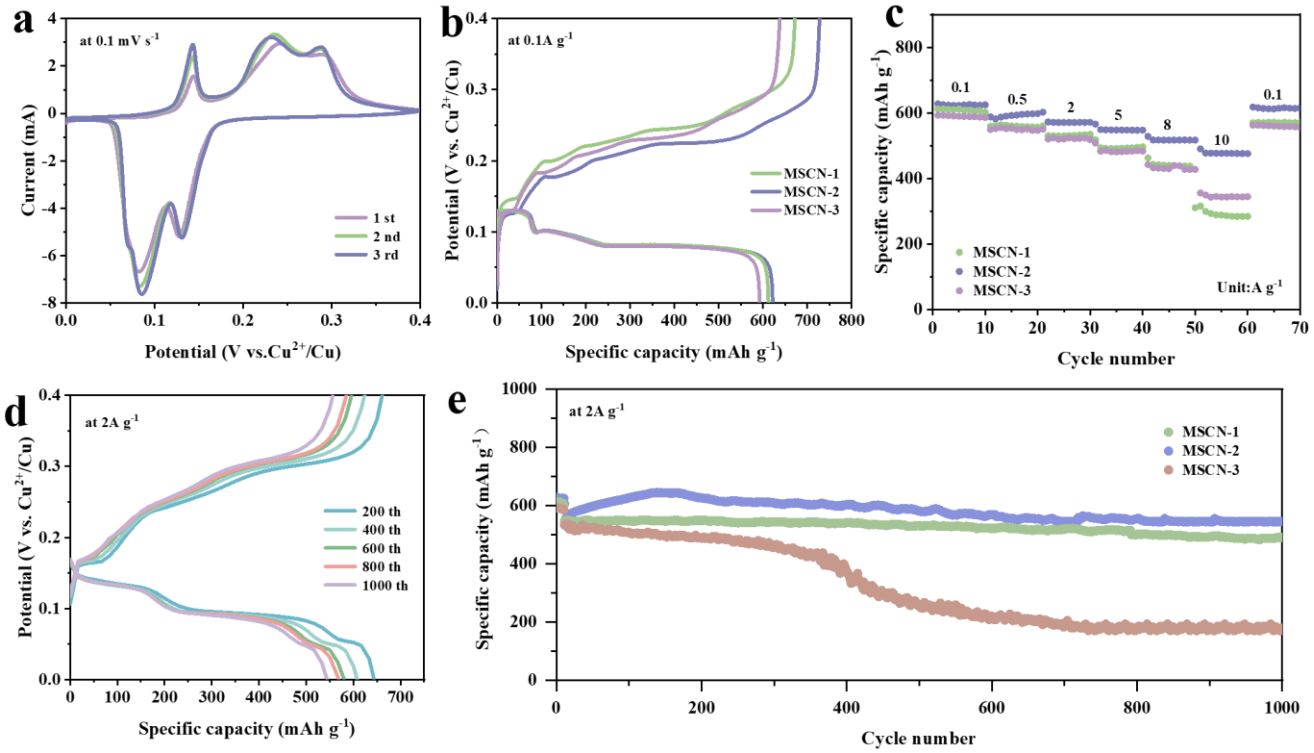

Figure 5. (**a**) The cyclic voltammetry (CV) curves of MSCN-2 during the initial three cycles. (**b**) Initial GCD curves at 0.1 A g^{-1} of the MSCN-x (x = 1, 2, 3). (**c**) Rate capability. (**d**) MSCN-2 GCD curves of different cycles. (**e**) Long-term cycling performance at 2 A g^{-1}.

The electrochemical performance of the MSCN-1, MSCN-2, and MSCN-3 electrodes was thoroughly evaluated, as illustrated in Figure 6. Electrochemical impedance spectroscopy (EIS) tests were performed on MSCN-x (x = 1, 2, 3) electrodes, with the resulting Nyquist plots displayed in Figure 6a. The impedance curve consists of two distinct com-

ponents: a semicircle observed at mid- and high-frequencies and a diagonal line at low frequencies. The high-frequency semicircle corresponds to the charge-transfer resistance, while the low-frequency diagonal line reflects the Warburg impedance. Notably, Among the electrodes, the MSCN-2 electrode demonstrates the lowest charge-transfer resistance (Rct) value of 1.15 Ω, in comparison to MSCN-1, with 1.53 Ω, and MSCN-3, with 6.37 Ω, indicating a more efficient charge-transfer process in the MSCN-2 electrode. Figure 6b presents the cyclic voltammetry (CV) curves of the MSCN-2 cathode material at various scan rates. Notably, two distinct sets of redox peaks can be observed, corresponding to the Cu^{2+} insertion/extraction processes. Additionally, as the scan rate increases, the polarization phenomenon causes the oxidation peaks to gradually shift to the right and the reduction peaks to the left, while the overall shape of the CV curves remains unchanged. The charge diffusion kinetics were analyzed using the equation $I = av^b$, where I represents the current, v is the scan rate, and a and b are fitting parameters. When the b value is close to 0.5, the reaction process is predominantly diffusion-controlled; when the b value approaches 1.0, it is controlled by pseudocapacitive behavior [53,54]. As shown in Figure 6c, the electrochemical reaction appears to be influenced by both pseudocapacitive behavior and diffusion, as indicated by the values close to 0.5. The pseudocapacitive and diffusion-controlled capacities can be calculated using the equation i = k1v + k2v1/2, where k1v and k2v1/2 represent the pseudocapacitive and diffusion contributions, respectively. Figure 6d illustrates the capacitance contribution of the MSCN-2 cathode material at different scan rates, increasing from 58% to 75% as the scan rate increases from 0.2 mV s^{-1} to 1.0 mV s^{-1}. Furthermore, according to the CV capacitance contribution curve at 0.2 mV s^{-1}, the capacitance contribution at this scan rate is determined to be 42% (Supplementary Figure S5).

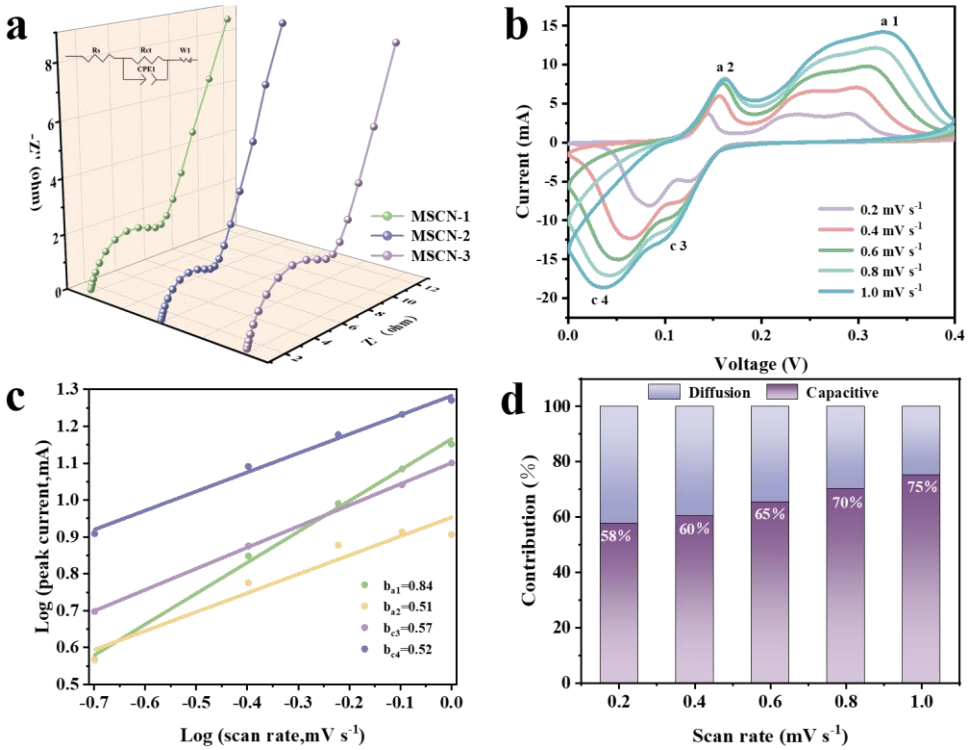

Figure 6. (**a**) Electrochemical impedance spectra (EIS) of MSCN-x (x = 1, 2, 3) electrodes. (**b**) CV curves of MSCN-2 at different scanning speeds. (**c**) Plots of log (i) vs. log (v) for Peak1~Peak 4 of MSCN-2. (**d**) Capacitive contribution ratios at different scan rates of MSCN-2.

To investigate the morphological evolution after different cycling intervals, the morphology of the MSCN-2 electrode in its pristine state, as well as after 300, 600, and 900 cycles, was analyzed using scanning electron microscopy (SEM), as illustrated in Figure 7a–d. In

the pristine state, the MSCN cubes were uniformly distributed on the collector electrode, with carbon nanotubes (CNTs) evenly wrapping the cubes' surfaces without any agglomeration, and there are no other impurities in the cube to indicate that the structure behaves more completely. The morphology of the MSCN-2 electrode after 300 cycles remained nearly unchanged compared to the original pristine sheet, However, despite the presence of some impurities and glass fibers around the cubes, the overall cubic structure remains unaffected, indicating robust structural stability during cycling. However, after 600 cycles, the MSCN-2 electrode exhibited slight chalking and agglomeration. The disruption of the cubic structure was the main reason for the degradation of its electrochemical properties. As charging and discharging continued, the pulverization of the morphology became more pronounced after 900 cycles, and the cubic structure had completely collapsed and was surrounded by impurities. The elemental distribution, depicted in Figure 7e, indicates the presence of Cu, in addition to Mn, Se, S, and C, within the electrode material, suggesting successful incorporation of Cu^{2+} ions into the MSCN-2 structure. According to the EDS total spectrum (Supplementary Figure S6), it can be clearly seen that the content of C is the most, accounting for 90.4%, and the remaining Cu and Mn account for 5.8% and 0.3%, respectively. It shows that the content of Cu^{2+} is increasing with the insertion and detachment of Cu^{2+} as the cycle proceeds, while the content of Mn is decreasing. During the cycling of the MSCN-2 electrodes, no cracking of the layers was observed. Considering the beneficial properties of Cu^{2+} storage and the protective role of CNTs in maintaining the cubic structure, it can be inferred that the use of MSCN-2 composites as electrodes enhances the durability of copper-ion batteries.

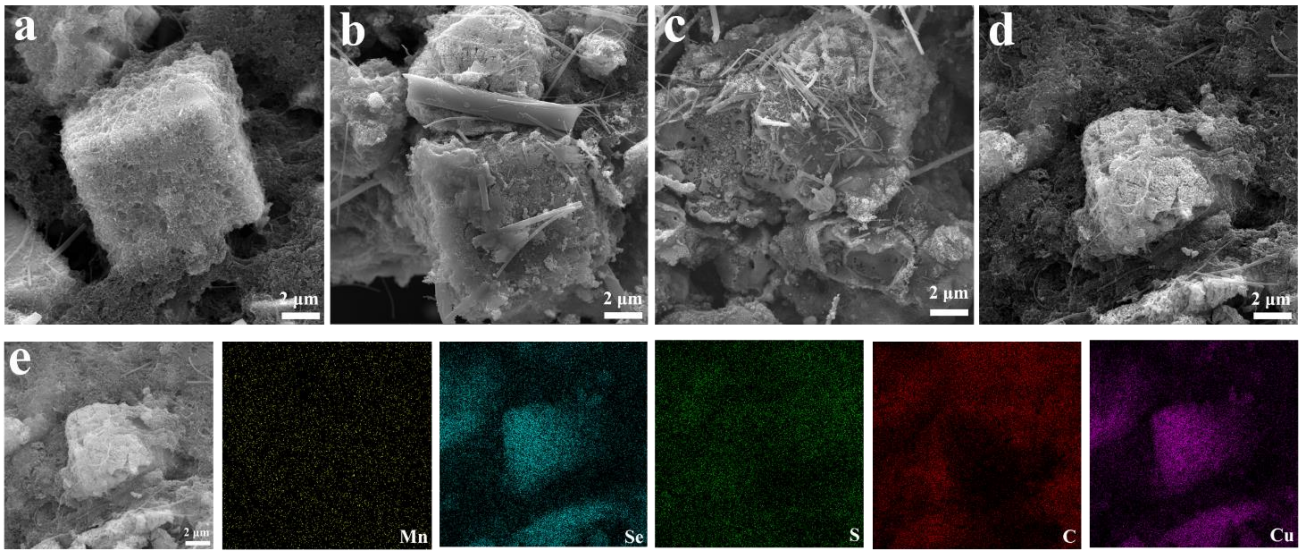

Figure 7. Scanning electron micrographs of the MSCN-2 electrode after varying numbers of charge–discharge cycles: (**a**) pristine, (**b**) 300 cycles, (**c**) 600 cycles, and (**d**) 900 cycles. (**e**) Energy-dispersive X-ray spectroscopy (EDS) mapping illustrating the elemental distribution on the electrode surface after 900 charge–discharge cycles.

4. Conclusions

In summary, three-dimensional cubic $MnSe_2$/CNTs composites were produced using a simple hydrothermal technique and efficiently utilized in aqueous copper-ion batteries. The synthesized composites exhibit a distinctive architecture, wherein the three-dimensional cubic $MnSe_2$ structures are uniformly encased by CNTs. The presence of CNTs does not alter the morphology and structure of $MnSe_2$; instead, their incorporation significantly enhances the electrical conductivity and mitigates volume changes, thereby ensuring the structural integrity of the composites. Among the $MnSe_2$/CNTs (MSCN) composites synthesized, the MSCN-2 composite demonstrated the lowest charge-transfer resistance (Rct), i.e., only

1.15 Ω. The initial discharge specific capacity was found to be 621 mAh g^{-1} at a current density of 0.1 A g^{-1}, and it maintained a significant specific capacity of 476 mAh g^{-1} even at 10 A g^{-1}. Furthermore, after 1000 cycles, the MSCN-2 composite maintained a specific capacity of 545 mAh g^{-1} at a current density of 2 A g^{-1}. This study underscores the potential of $MnSe_2$/CNTs electrodes as a viable strategy for the development of high-performance aqueous copper-ion battery cathode materials.

Supplementary Materials: The following supporting information can be downloaded at https://www.mdpi.com/article/10.3390/nano14201621/s1, Figure S1: SEM images of $MnSe_2$; Figure S2: The cyclic voltammetry (CV) curves of MSCN-1 during the initial three cycles; Figure S3: The cyclic voltammetry (CV) curves of MSCN-3 during the initial three cycles; Figure S4: GCD curves at 0.1 A g^{-1} of the $MnSe_2$; Figure S5: Capacitive contribution at 0.2 mV s^{-1}; Figure S6: EDS Sum Spectrum of MSCN-3; Figure S7: EDS Sum Spectrum of MSCN-2.

Author Contributions: Conceptualization, J.L., W.Z., H.C. and S.J.; methodology, J.W. and L.T.; validation, J.W., L.T. and W.Z.; formal analysis, J.W., L.T. and H.C.; investigation, J.W. and J.L.; data curation, W.Z. and H.C.; writing—original draft preparation, J.W.; writing—review and editing, J.L. and S.J.; supervision, J.L. and S.J.; project administration, J.L. and S.J.; funding acquisition, J.L. All authors have read and agreed to the published version of the manuscript.

Funding: This research was funded by the National Natural Science Foundation of China (52171200, 52371211) and Changsha Special Project (kh2301006), Excellent youth funding of Hunan Provincial Education Department (22B0588), Key research and development project of Hunan Province (2022GK2049), and National Sustainable Development Innovation Demonstration Zone project (2022sfq09).

Data Availability Statement: The original contributions presented in the study are included in the article/Supplementary Material, further inquiries can be directed to the corresponding authors.

Conflicts of Interest: The authors declare no conflicts of interest.

References

1. Fan, X.; Xiang, K.; Zhou, W.; Deng, W.; Zhu, H.; Chen, L.; Chen, H. A novel improvement strategy and a comprehensive mechanism insight for α-MnO_2 energy storage in rechargeable aqueous zinc-ion batteries. *Carbon Energy* **2024**, *6*, e536. [CrossRef]
2. Guo, Z.; Han, X.; Zhang, C.; He, S.; Liu, K.; Hu, J.; Yang, W.; Jian, S.; Jiang, S.; Duan, G. Activation of biomass-derived porous carbon for supercapacitors: A review. *Chin. Chem. Lett.* **2024**, *35*, 109007. [CrossRef]
3. Shang, Z.; An, X.; Nie, S.; Li, N.; Cao, H.; Cheng, Z.; Liu, H.; Ni, Y.; Liu, L. Design of B/N Co-doped micro/meso porous carbon electrodes from CNF/BNNS/ZIF-8 nanocomposites for advanced supercapacitors. *J. Bioresour. Bioprod.* **2023**, *8*, 292–305. [CrossRef]
4. Guo, F.; He, W.; Wang, R.; Wei, B.; Liang, S.; Qiulin, J.; Hu, G.; Li, W. Preparation of nano-structured wood aerogel-based composite electrode and its electrochemical performance. *J. For. Eng.* **2023**, *8*, 122–130. [CrossRef]
5. Yang, J.; Wang, Y.; Liu, Y.; Duan, G.; Liang, Z.; Han, J.; Huang, Y.; Han, X.; Zhang, C.; He, S.; et al. Design of cyclic carbonate-based electrolytes for HC anodes towards improved low-temperature performance in lithium-ion batteries system. *Fuel* **2025**, *379*, 133048. [CrossRef]
6. Wen, X.; Luo, J.; Xiang, K.; Zhou, W.; Zhang, C.; Chen, H. High-performance monoclinic WO_3 nanospheres with the novel NH_4^+ diffusion behaviors for aqueous ammonium-ion batteries. *Chem. Eng. J.* **2023**, *458*, 141381. [CrossRef]
7. Huang, Y.-z.; Xing, L.; Pei, S.; Zhou, W.; Hu, Y.-j.; Deng, W.-N.; Chen, L.; Zhu, H.; Chen, H. Co_9S_8/CNTs microspheres as superior-performance cathodes in aqueous ammonium-ion batteries. *Trans. Nonferrous Met. Soc. China* **2023**, *33*, 3452–3464. [CrossRef]
8. Guo, T.; Xiang, K.; Wen, X.; Zhou, W.; Chen, H. Facile construction on flower-like CuS microspheres and their applications for the high-performance aqueous ammonium-ion batteries. *Mater. Res. Bull.* **2024**, *170*, 112595. [CrossRef]
9. Liu, Y.; Xiang, K.; Zhou, W.; Deng, W.; Zhu, H.; Chen, H. Investigations on Tunnel-Structure MnO_2 for Utilization as a High-Voltage and Long-Life Cathode Material in Aqueous Ammonium-Ion and Hybrid-Ion Batteries. *Small* **2024**, *20*, 2308741. [CrossRef]
10. Jiang, S.; Liu, H.; Zhang, W.; Lu, Y. Bioanode boosts efficacy of chlorobenzenes-powered microbial fuel cell: Performance, kinetics, and mechanism. *Bioresour. Technol.* **2024**, *405*, 130936. [CrossRef]
11. Li, L.; Nam, J.S.; Kim, M.S.; Wang, Y.; Jiang, S.; Hou, H.; Kim, I.D. Sulfur–Carbon Electrode with PEO-LiFSI-PVDF Composite Coating for High-Rate and Long-Life Lithium–Sulfur Batteries. *Adv. Energy Mater.* **2023**, *13*, 2302139. [CrossRef]

12. Tian, Z.; Yang, C.; Zhang, C.; Han, X.; Han, J.; Liu, K.; He, S.; Duan, G.; Jian, S.; Hu, J.; et al. In-situ activation of resorcinol-furfural resin derived hierarchical porous carbon for supercapacitors and zinc-ion hybrid capacitors. *J. Energy Storage* **2024**, *85*, 111130. [CrossRef]
13. Andrade, A.M.; Liu, Z.; Grewal, S.; Nelson, A.J.; Nasef, Z.; Diaz, G.; Lee, M.H. MOF-derived Co/Cu-embedded N-doped carbon for trifunctional ORR/OER/HER catalysis in alkaline media. *Dalton Trans.* **2021**, *50*, 5473–5482. [CrossRef]
14. Jiang, L.; Wu, Z.; Wang, Y.; Tian, W.; Yi, Z.; Cai, C.; Jiang, Y.; Hu, L. Ultrafast zinc-ion diffusion ability observed in 6.0-nanometer spinel nanodots. *ACS Nano* **2019**, *13*, 10376–10385. [CrossRef]
15. Wang, L.; Shi, J.L.; Su, H.; Li, G.; Zubair, M.; Guo, Y.G.; Yu, H. Composite-structure material design for high-energy lithium storage. *Small* **2018**, *14*, 1800887. [CrossRef]
16. Zhang, H.; Yao, Z.; Lan, D.; Liu, Y.; Ma, L.; Cui, J. N-doped carbon/V_2O_3 microfibers as high-rate and ultralong-life cathode for rechargeable aqueous zinc-ion batteries. *J. Alloys Compd.* **2021**, *861*, 158560. [CrossRef]
17. Liu, Y.-Y.; Lv, T.-T.; Wang, H.; Guo, X.-T.; Liu, C.-S.; Pang, H. Nsutite-type VO_2 microcrystals as highly durable cathode materials for aqueous zinc-Ion batteries. *Chem. Eng. J.* **2021**, *417*, 128408. [CrossRef]
18. Liang, Y.; Dong, H.; Aurbach, D.; Yao, Y. Current status and future directions of multivalent metal-ion batteries. *Nat. Energy* **2020**, *5*, 646–656. [CrossRef]
19. Wang, D.; Lv, H.; Hussain, T.; Yang, Q.; Liang, G.; Zhao, Y.; Ma, L.; Li, Q.; Li, H.; Dong, B. A manganese hexacyanoferrate framework with enlarged ion tunnels and two-species redox reaction for aqueous Al-ion batteries. *Nano Energy* **2021**, *84*, 105945. [CrossRef]
20. Cai, H.; Bi, S.; Wang, R.; Liu, L.; Niu, Z. A lattice-matching strategy for highly reversible copper-metal anodes in aqueous batteries. *Angew. Chem. Int. Ed.* **2022**, *61*, e202205472. [CrossRef]
21. Yang, Z.; Xu, C.; Yan, H.; Liu, Y.; Yue, C.; Zhang, L.; Shui, M.; Hu, F.; Shu, J. Laser-induced graphene assisting self-conversion reaction for sulfur-free aqueous Cu-S battery. *Adv. Funct. Mater.* **2021**, *31*, 2103893. [CrossRef]
22. Wu, X.; Markir, A.; Ma, L.; Xu, Y.; Jiang, H.; Leonard, D.P.; Shin, W.; Wu, T.; Lu, J.; Ji, X. A four-electron sulfur electrode hosting a Cu^{2+}/Cu^{+} redox charge carrier. *Angew. Chem. Int. Ed.* **2019**, *58*, 12640–12645. [CrossRef] [PubMed]
23. Zhang, J.; Wang, Y.; Yu, M.; Ni, J.; Li, L. Understanding the role of topotactic anion exchange in the robust Cu ion storage of CuS1–x Se x. *ACS Energy Lett.* **2022**, *7*, 1835–1841. [CrossRef]
24. Javed, M.S.; Najim, T.; Hussain, I.; Batool, S.; Idrees, M.; Mehmood, A.; Imran, M.; Assiri, M.A.; Ahmad, A.; Shah, S.S.A. 2D V_2O_5 nanoflakes as a binder-free electrode material for high-performance pseudocapacitor. *Ceram. Int.* **2021**, *47*, 25152–25157. [CrossRef]
25. Liu, Y.; Wang, Z.; Zhong, Y.; Tade, M.; Zhou, W.; Shao, Z. Molecular design of mesoporous $NiCo_2O_4$ and $NiCo_2S_4$ with sub-micrometer-polyhedron architectures for efficient pseudocapacitive energy storage. *Adv. Funct. Mater.* **2017**, *27*, 1701229. [CrossRef]
26. Javed, M.S.; Najam, T.; Hussain, I.; Shah, S.S.A.; Ibraheem, S.; Mahmood, A.; Imran, M.; Assiri, M.A.; Siyal, S.H. Novel 2D vanadium oxysulfide nano-spindles decorated carbon textile composite as an advanced electrode for high-performance pseudocapacitors. *Mater. Lett.* **2021**, *303*, 130478. [CrossRef]
27. Hussain, I.; Mohamed, S.G.; Ali, A.; Abbas, N.; Ammar, S.M.; Al Zoubi, W. Uniform growth of Zn-Mn-Co ternary oxide nanoneedles for high-performance energy-storage applications. *J. Electroanal. Chem.* **2019**, *837*, 39–47. [CrossRef]
28. Dan, H.; Tao, K.; Hai, Y.; Liu, L.; Gong, Y. (Co, Mn)-Doped $NiSe_2$-diethylenetriamine (dien) nanosheets and (Co, Mn, Sn)-doped $NiSe_2$ nanowires for high performance supercapacitors: Compositional/morphological evolution and (Co, Mn)-induced electron transfer. *Nanoscale* **2019**, *11*, 16810–16827. [CrossRef]
29. Ni, D.; Chen, Y.; Yang, X.; Liu, C.; Cai, K. Microwave-assisted synthesis method for rapid synthesis of tin selenide electrode material for supercapacitors. *J. Alloys Compd.* **2018**, *737*, 623–629. [CrossRef]
30. Ali, L.; Shittu, T.; Kuttiyathil, M.S.; Alam, A.; Iqbal, M.Z.; Khaleel, A.; Sivaramakrishnan, K.; Altarawneh, M. Catalytic upgrading of bio-oil from halophyte seeds into transportation fuels. *J. Bioresour. Bioprod.* **2023**, *8*, 444–460. [CrossRef]
31. Sree Raj, K.; Shajahan, A.S.; Chakraborty, B.; Rout, C.S. Two-dimensional layered metallic VSe_2/SWCNTs/rGO based ternary hybrid materials for high performance energy storage applications. *Chem.—A Eur. J.* **2020**, *26*, 6662–6669. [CrossRef]
32. Li, M.; Bai, L.; Jiang, S.; Sillanpää, M.; Huang, Y.; Liu, Y. Electrocatalytic transformation of oxygen to hydroxyl radicals via three-electron pathway using nitrogen-doped carbon nanotube-encapsulated nickel nanocatalysts for effective organic decontamination. *J. Hazard. Mater.* **2023**, *452*, 131352. [CrossRef]
33. Rout, C.S.; Mondal, S.; Samal, R.; Gangan, A.S.; Nayak, S.K.; Chakraborty, B. An experimental and computational study of enhanced charge storage capacity of chemical vapor deposited Ni_3S_2-reduced graphene oxide hybrids. *Appl. Surf. Sci.* **2019**, *497*, 143789. [CrossRef]
34. Jiang, S.; Xie, M.; Jin, L.; Ren, Y.; Zheng, W.; Ji, S.; Liu, Y. New insights into electrocatalytic singlet oxygen generation for effective and selective water decontamination. *Chin. Chem. Lett.* **2024**. [CrossRef]
35. Samal, R.; Mondal, S.; Gangan, A.S.; Chakraborty, B.; Rout, C.S. Comparative electrochemical energy storage performance of cobalt sulfide and cobalt oxide nanosheets: Experimental and theoretical insights from density functional theory simulations. *Phys. Chem. Chem. Phys.* **2020**, *22*, 7903–7911. [CrossRef]
36. Shi, X.; Wang, H.; Ji, S.; Linkov, V.; Liu, F.; Wang, R. $CoNiSe_2$ nanorods directly grown on Ni foam as advanced cathodes for asymmetric supercapacitors. *Chem. Eng. J.* **2019**, *364*, 320–327. [CrossRef]

37. Pathak, M.; Tamang, D.; Kandasamy, M.; Chakraborty, B.; Rout, C.S. A comparative experimental and theoretical investigation on energy storage performance of $CoSe_2$, $NiSe_2$ and $MnSe_2$ nanostructures. *Appl. Mater. Today* **2020**, *19*, 100568. [CrossRef]
38. Dong, H.; Li, X.; Niu, L.; Liu, Z. Preparation and electrochemical performance of nanocellulose/carbon nanotube carbon aerogel. *J. For. Eng.* **2023**, *8*, 121–129. [CrossRef]
39. Javed, M.S.; Shah, S.S.A.; Hussain, S.; Tan, S.; Mai, W. Mesoporous manganese-selenide microflowers with enhanced electrochemical performance as a flexible symmetric 1.8 V supercapacitor. *Chem. Eng. J.* **2020**, *382*, 122814. [CrossRef]
40. Momma, T.; Liu, X.; Osaka, T.; Ushio, Y.; Sawada, Y. Electrochemical modification of active carbon fiber electrode and its application to double-layer capacitor. *J. Power Sources* **1996**, *60*, 249–253. [CrossRef]
41. Samal, R.; Bhat, M.; Kapse, S.; Thapa, R.; Late, D.J.; Rout, C.S. Enhanced energy storage performance and theoretical studies of 3D cuboidal manganese diselenides embedded with multiwalled carbon nanotubes. *J. Colloid Interface Sci.* **2021**, *598*, 500–510. [CrossRef]
42. Ma, W.; Ding, Y.; Li, Y.; Gao, S.; Jiang, Z.; Cui, J.; Huang, C.; Fu, G. Durable, self-healing superhydrophobic nanofibrous membrane with self-cleaning ability for highly-efficient oily wastewater purification. *J. Membr. Sci.* **2021**, *634*, 119402. [CrossRef]
43. Cao, J.; He, W.; Zhou, P.; Wei, B.; Wang, R.; Liang, S.; Ji, Q. Preparation of wood aerogel membrane and adsorption performance on Cu^{2+} in waste water. *J. For. Eng.* **2023**, *8*, 113–120. [CrossRef]
44. Lu, T.; Liang, H.; Cao, W.; Deng, Y.; Qu, Q.; Ma, W.; Xiong, R.; Huang, C. Blow-spun nanofibrous composite Self-cleaning membrane for enhanced purification of oily wastewater. *J. Colloid Interface Sci.* **2022**, *608*, 2860–2869. [CrossRef] [PubMed]
45. Deng, Y.; Lu, T.; Zhang, X.; Zeng, Z.; Tao, R.; Qu, Q.; Zhang, Y.; Zhu, M.; Xiong, R.; Huang, C. Multi-hierarchical nanofiber membrane with typical curved-ribbon structure fabricated by green electrospinning for efficient, breathable and sustainable air filtration. *J. Membr. Sci.* **2022**, *660*, 120857. [CrossRef]
46. Xie, J.; Liu, G.; Sun, J.; Zheng, R.; Zhao, W.; Chu, T.; Lin, H.; Xu, Y.; Gao, S.; Sui, Z. α-MnO_2/CNTs with cross-linked reticular structure: Towards ultralong life zinc-ion batteries. *Diam. Relat. Mater.* **2022**, *125*, 109024. [CrossRef]
47. Xu, C.; Peng, S.; Tan, C.; Ang, H.; Tan, H.; Zhang, H.; Yan, Q. Ultrathin S-doped $MoSe_2$ nanosheets for efficient hydrogen evolution. *J. Mater. Chem. A* **2014**, *2*, 5597–5601. [CrossRef]
48. Xie, J.; Liu, G.; Jiang, X.; Sui, Z.; Gao, S. One-step co-precipitation of $MnSe_2$/CNTs as a high-performance cathode material for zinc-ion batteries. *Ceram. Int.* **2023**, *49*, 10165–10171. [CrossRef]
49. Zhu, H.; Qin, G.; Zhou, W.; Li, Y.; Zhou, X. Constructing flake-like ternary rare earth $Pr_3Si_2C_2$ ceramic on SiC whiskers to enhance electromagnetic wave absorption properties. *Ceram. Int.* **2024**, *50*, 134–142. [CrossRef]
50. Qu, Q.; Zhang, X.; Yang, A.; Wang, J.; Cheng, W.; Zhou, A.; Deng, Y.; Xiong, R.; Huang, C. Spatial confinement of multi-enzyme for cascade catalysis in cell-inspired all-aqueous multicompartmental microcapsules. *J. Colloid Interface Sci.* **2022**, *626*, 768–774. [CrossRef]
51. Zhu, L.; Li, Y.; Zhao, J.; Liu, J.; Lei, J.; Wang, L.; Huang, C. A novel green lignosulfonic acid/Nafion composite membrane with reduced cost and enhanced thermal stability. *Chem. Commun.* **2021**, *57*, 9288–9291. [CrossRef] [PubMed]
52. Zhou, W.; Zeng, G.; Jin, H.; Jiang, S.; Huang, M.; Zhang, C.; Chen, H. Bio-Template Synthesis of V_2O_3@ Carbonized Dictyophora Composites for Advanced Aqueous Zinc-Ion Batteries. *Molecules* **2023**, *28*, 2147. [CrossRef] [PubMed]
53. Deng, Q.; Liu, X.; Li, Z.; Fan, H.; Zhang, Y.; Yang, H.Y. Cobalt-nickel bimetallic sulfide (NiS_2/CoS_2) based dual-carbon framework for super sodium ion storage. *J. Colloid Interface Sci.* **2023**, *633*, 480–488. [CrossRef]
54. Li, X.; Liang, H.; Qin, B.; Wang, M.; Zhang, Y.; Fan, H. Rational design of heterostructured bimetallic sulfides (CoS_2/NC@VS_4) with VS_4 nanodots decorated on CoS_2 dodecahedron for high-performance sodium and potassium ion batteries. *J. Colloid Interface Sci.* **2022**, *625*, 41–49. [CrossRef] [PubMed]